On the Spatial Variability of the Sea Surface Height Wavenumber Spectra in the Atlantic Ocean

Xiaobiao Xu[1], Eric P. Chassignet[1], Alan J. Wallcraft[1], Brian K. Arbic[2],

Maarten C. Buijsman[3], and Miguel Solano[3]

[1] Center for Ocean-Atmospheric Prediction Studies (COAPS), Florida State University

[2] Department of Earth and Environmental Sciences, University of Michigan

[3] School of Ocean Science and Engineering, University of Southern Mississippi

A manuscript submitted to JGR Oceans

Key Points

1. The slope of the sea surface height (SSH) power spectra as derived from satellite observations exhibits a large spatial variability, which is now reproduced in numerical ocean models.
2. The surface manifestation of internal tides is the main driver for spatial variability in the slope of the SSH power spectra.
3. High-resolution bathymetry plays an important role in the internal tide generation locally but has a relatively small impact on the SSH power spectra on a broader scale.

Abstract

The wavenumber spectral slope of sea surface height (SSH) computed within the mesoscale range from satellite altimetry exhibits a large spatial variability which, until now, has not been reproduced in numerical ocean models. This study documents the impacts of including internal tides, high-resolution bathymetry, and high-frequency atmospheric variability on the SSH wavenumber spectra in the Atlantic Ocean, using a series of 1/50° Equatorial and North Atlantic simulations with a realistic representation of barotropic/baroclinic tides and mesoscale-to-submesoscale variability. The results show that the inclusion of internal tides does increase high frequency SSH variability (with clear peaks near 120 km and 70 km) and flattens the spectra slope in the mesoscale range in a good agreement with observations. The surface signature of internal tides, mostly in the equatorial Atlantic but also in subtropical regions in the eastern North Atlantic, is the primary reason behind the observed large spatial variability of the spectral slope in the Atlantic. Internal tides are stronger in the tropical regions when compared to higher latitudes because of the stronger barotropic tides and stronger stratification in the upper layer of the water column. High-resolution bathymetry does play an important role in the internal tide generation on a local scale, but its impact on large-scale SSH variability and SSH wavenumber spectra is quite small. High-frequency wind variability plays only a minor role on the generation of high-frequency SSH variability.

Plain Language Summary

The sea surface height (SSH) wavenumber spectrum is a quantification of the magnitude of SSH variability on different spatial scales. The slope of SSH wavenumber spectra is essential to understanding how kinetic energy is transferred across different scales in the turbulent ocean. The most striking feature of the SSH spectral slope as derived from satellite observations is that it has a wide range of values over different parts of the Atlantic Ocean: from an order of -5 in the western boundary current, to an order of -4 to -3 in the interior of subtropical North Atlantic, and to an order of -1 to -0.5 in the tropical Atlantic. In this study, we reproduced the observed spatial variability of the SSH spectral slope in numerical ocean models, and further documented that internal tide is the main driver behind the scenes. The surface manifestation of internal tides flattens the spectral slope of the SSH. This flattening is most significant in the tropical Atlantic, but also occurs in the subtropical eastern North Atlantic. The impacts from other factors such as high-resolution bathymetry and high-frequency atmospheric forcing are relatively small.

1. Introduction

Kinetic energy (KE) in the ocean is dominated by mesoscale eddy variability with a spatial scale of tens to hundreds of kilometers and a temporal scale of tens to hundreds of days (e.g., Wyrtki et al., 1976; Richardson, 1983; Decut et al., 2000; Frantantoni, 2001). The mechanisms that control the transfer of kinetic energy across different spatial scales are, however, still not fully understood (Ferrari and Wunsch, 2009, 2010) and different theories have been put forward on the physics responsible for mesoscale energy cascades in the ocean. On one hand, the quasigeostrophic (QG) turbulence theory (Charney 1971; Hua and Haidvogel 1986; McWilliams, 1989; Smith and Vallis, 2001) predicts a k^{-3} power law for the KE wavenumber spectrum (wavenumber k is $1/\lambda$, where λ is the wavelength). On the other hand, the surface quasigeostrophic (SQG) theory (Blumen, 1978; Held et al., 1995; LaCasce and Mahadevan, 2006; Isern-Fontanet et al., 2006; Lapeyre and Klein, 2006; Capet et al., 2008) predicts a power law of $k^{-5/3}$.

Satellite altimetry, which measures the sea surface height (SSH) globally and repeatedly, allows us to examine the question as to whether which dynamical explanation, i.e., QG (power law of k^{-5}) or SQG (power law of $k^{-11/3}$), is pertinent to describe geostrophic ocean turbulence (note that the SSH wavenumber spectra are equivalent to the KE wavenumber spectra multiplied by k^{-2} when assuming geostrophic balance). Several studies computed the SSH wavenumber spectra from altimetry (e.g., Fu, 1983, Le Traon et al., 1990, 2008; Wunsch and Stammer, 1995; Strammer, 1997; Xu and Fu, 2011, 2012; Zhou et al., 2015; Dufau et al., 2016) and a clear outcome, despite differences in the methods used to remove measurement errors and noises, is that there is a large variability in the spatial distribution of the slope of the SSH spectra. In the mesoscale range of 70-250 km, the estimated slope derived from satellite altimetry is close to -5 (i.e., QG theory) in the high-EKE regions (western boundary current and/or the Antarctic circumpolar current), whereas

in the low-EKE ocean interior, it is about -3, which is close to but somewhat flatter than what is derived from SQG theory. In-situ measurements of ocean currents with shipboard acoustic Doppler current profiler (ADCP) have been used to directly calculate the wavenumber spectra of the near surface KE (Wang et al., 2010; Callies and Ferrari, 2013; Rocha et al., 2016; Qiu et al., 2017). Despite being limited to a few places where repeat surveys are available, the general picture is consistent with that based on altimetry, in that the spectral slope is steep and close to that of the QG theory in the high-EKE regions and is flatter and closer to the SQG theory in the low-EKE regions.

The most striking feature, however, regarding the spatial variability of the SSH wavenumber spectral slope is not the difference in slope between the high EKE boundary current and low EKE ocean interior, but the difference between high/mid-latitudes and the equator (e.g., Xu and Fu, 2011, 2012; Zhou et al., 2015, Dufau et al., 2016). Specifically, the SSH wavenumber slope in the equatorial Atlantic Ocean is much flatter (on the order of -0.5 to -1) than in the Gulf Stream region (on the order of -5). These values of -0.5 to -1 near the equator are much flatter than either values predicted by QG or SQG turbulence theories; they are also not found in the SSH spectra computed using outputs from a series of numerical simulations with resolutions ranging from 1/12° to 1/50° (Paiva et al., 1999; Sasaki and Klein, 2012; Chassignet and Xu, 2017). This discrepancy between the observations and the models suggests that either a) these numerical simulations underestimate or do not resolve high-frequency motions, such as internal waves/tides (Chassignet and Xu, 2021), or b) the altimetry data contains noise and/or are aliased (Wang et al., 2010; Zhou et al., 2015; Biri et al., 2016), or a combination of both.

The main goal of this paper is to systematically document what factors or processes control the spatial variability of the SSH wavenumber spectra in the Atlantic Ocean, using observations from

altimetry as a guide. Internal tides have been put forward as one the potential leading factor that could flatten the SSH spectra slope in numerical models (e.g., Richman et al., 2012; Rocha et al., 2016; Savage et al., 2017; Chassignet and Xu, 2021) and Tchilibou et al. (2018) recently demonstrated that, in a small regional model of the eastern Solomon Sea in the southwest Pacific equatorial region, internal tides can flatten the modeled SSH spectra slope to a value close to observations. It remains unclear, however, if this is valid across the entire equatorial region and/or beyond to the extratropical latitudes. Richman et al. (2012) did not find a noticeable reduction in the SSH spectra slope across the equatorial Pacific due to internal tides, except for small regions near the western and eastern boundaries. In addition to tides, other factors such as a lack of high-frequency atmospheric forcing or high-resolution bathymetry could also contribute to a lower SSH variability on small scales in numerical models, and hence a steeper slope in wavenumber spectra. In the observations, noise and one-dimensional (1-D) sampling aliasing in the altimetry could potentially lead to an underestimation of the slope (Xu and Fu, 2012; Zhou et al., 2015).

The paper is organized as follows. Section 2 summarizes the basic configurations of the numerical simulations used in this study and the implementation of tides. Section 3 focuses on the surface manifestation of the high-frequency motions in the numerical experiments. Section 4 discusses how the increase in high-frequency variability is reflected in the SSH wavenumber spectra. Section 5 examines the impacts of temporal/spatial resolution and 1-D sampling (of the satellite altimetry observations) on wavenumber spectra calculations. Finally, the key findings are summarized and discussed in Section 6.

2. Numerical Simulations

In this section, we first briefly summarize the configurations of the five North and Equatorial Atlantic (NEATL) experiments that are used to systematically document the impact of tides, high-

resolution bathymetry, and high frequency atmospheric forcing on SSH variability. Then we describe how the tidal forcing is implemented in the simulations and the realism of our modeled barotropic tides with respect to well-established tidal models and global simulations.

a. Basic Configurations

The North and Equatorial Atlantic experiments used in this study are part of a suite of eddying numerical simulations performed with the Hybrid Coordinate Ocean Model (HYCOM, Bleck 2002; Chassignet et al., 2003) to study the large-scale circulation and water mass transformations in the Atlantic; see Chassignet and Xu (2017) and the references therein for a detailed discussion. We focus on the 1/50° simulations because this resolution gives the best representation of the western boundary current (e.g., the Gulf Stream) penetration and associated mesoscale and sub-mesoscale eddy variability (Chassignet and Xu, 2017, 2021). Five experiments are considered (Table 1), all with the same vertical resolution of 32 layers:

1) NEATL is the non-tidal 1/50° reference simulation discussed in Chassignet and Xu (2017) with 6-hourly atmospheric forcing. This simulation is integrated for 20 years, and the diagnostics are performed over the last 5 years. The bathymetry of this NEATL simulation was interpolated from a 1/12° configuration to investigate the impact of horizontal resolution and thus does not include fine-resolution bathymetry details.
2) NEATL-HB is therefore a twin experiment of NEATL, but with a high-resolution bathymetry that is derived from the 2019 version of the 15-second General Bathymetric Chart of the Ocean dataset (GEBCO_2019). This simulation is restarted from NEATL at the beginning of year 16 and is integrated for 5 years.

3) NEATL-T is a twin experiment of NEATL, but with tides. This simulation is restarted from NEATL at the beginning of year 16 and is integrated for 18 months (with 8 tidal constituents), and the last 12 months outputs are used in the analysis.

4) NEATL-T-HB is twin of NEATL-HB with tides. This simulation is restarted from NEATL-HB at the beginning of year 19 to allow the adjustment of the high-resolution bathymetry and is, as NEATL-T, integrated for 18 months, with the last 12 months outputs used for analysis.

5) NEATL-T-HB-HF is a twin of the NEATL-T-HB with hourly high-frequency atmospheric forcing. This simulation is also restarted from NEATL-HB at the beginning of year 19 and integrated for 18 months, but it now includes tides and hourly wind stress variability from the Climate Forecast System Reanalysis (CFSR), in contrast to the 6-hourly atmospheric forcing variability used in the previous four experiments.

Table 1. Summary of five 1/50° Atlantic HYCOM simulations with and without tides

Experiment Label	Description
NEATL	No tides, bathymetry from 1/12°, 6-hourly atmospheric forcing
NEATL-HB	Twin of NEATL, with high-resolution bathymetry
NEATL-T	Twin of NEATL, with 8 tidal constituents
NEATL-T-HB	Twin of NEATL-HB, with 8 tidal constituents
NEATL-T-HB-HF	Twin of NEATL-T-HB, with hourly atmospheric forcing

b. Implementation of Tides

Simulating the eddying general circulation simultaneously with barotropic and baroclinic tides is non-trivial; see Arbic et al. (2010, 2012, 2018), Shriver et al. (2012), and Buijsman et al. (2020) for a discussion on the implementation and evaluation of tides in global HYCOM simulations. To

implement tides in a general circulation model, one needs to consider 1) the tidal forcing and 2) the tidal dissipation. For tidal forcing, the North and Equatorial Atlantic HYCOM simulations include the eight largest tidal constituents (K_1, O_1, P_1, Q_1, M_2, S_2, N_2, and K_2), driven by both the astronomical tidal potential (corrected for solid earth body tides) and the barotropic tides (bottom pressure and velocity), based upon the TPXO8 atlas (Egbert and Erofeeva, 2002) passing through the NEATL northern and southern boundaries. There is no atmospheric pressure loading. Amplitude and phase maps of self-attraction and loading (SAL, Ray, 1998) are taken from the TPXO8 atlas and applied as an additional tidal forcing term. The SAL term incorporates the compression and expansion of the solid earth due to the load of the ocean tide, and the perturbation gravitational potential due to the self-gravitation of both the ocean tide itself and the load-deformed solid earth.

For dissipation, the North and Equatorial Atlantic HYCOM simulations include a quadratic bottom drag which primarily dissipates tidal energy in coastal regions, where tidal velocities are high. Barotropic tidal models typically include a linear bottom drag that is intended to parameterize the conversion of external tides to internal tides (which do not exist in a barotropic model). The location and relative strength of this so-called internal wave drag can be determined in various ways, with the first approach by Jayne and St. Laurent (2001) still being popular, but all approaches include a scalar multiplicative factor that in practice is used to tune the wave drag to give the best fit to the observed tide (Buijsman, 2015, 2020). Since baroclinic models resolve some of the internal wave spectrum (low mode), they may have less need for a parameterized internal wave drag. But HYCOM, as a hydrostatic model, may still need some wave drag to account for the unresolved conversion from low mode to high mode internal tides and to dampen internal waves

(Ansong et al., 2015; Buijsman et al., 2016; 2020). We took the pragmatic approach of continuing to tune wave drag as in Arbic et al. (2010) to fit the observed tides.

c. Representation of Barotropic Tides

For global HYCOM simulations with 1/12° horizontal resolution, the best case of barotropic tide representation, measured by the lowest M_2 root mean square (RMS) error when compared to TPXO8 atlas, was found to occur with a wave drag scale of 0.5, which is less than in the corresponding barotropic model, but is not zero (Ngodock, 2016). For Atlantic HYCOM simulations performed at the same 1/12° horizontal resolution, prescribing the observed barotropic tides at the open boundaries significantly improves the tides when compared to the 1/12° global simulations for the same wave drag. Figures 1a-b compares the M_2 RMS error in 1/12° global and Atlantic simulations, in which the domain-averaged error is 5.8 cm and 2.6 cm, respectively. We further found that the RMS error in the Atlantic simulations decreases slightly with less wave drag: the domain-averaged error is 2.8, 2.6, 2.3, and 2.2 cm for a wave drag scale of 0.75, 0.50, 0.25, and 0, respectively. Thus, the wave drag is set to zero for all the 1/50° Atlantic tide simulations discussed in this paper.

It is also generally expected that numerical solutions (including the barotropic tides) will improve with finer horizontal resolutions. Figures 1c-d display the M_2 RMS error represented in two of the 1/50° simulations: NEATL-T in which the bathymetry is linearly interpolated from 1/12° model (Figure 1c) and NEATL-T-HB with the high-resolution 1/50° resolution bathymetry (Figure 1d). An increase in the resolution alone from 1/12° to 1/50° does not improve the representation of the barotropic tides: in some areas the error is slightly higher in the 1/50° NEATL-T than that in the 1/12° simulation (Figures 1b & 1c). However, the representation of barotropic tides is dramatically improved in the NEATL-T-HB when high-resolution bathymetry and coastline are included

(Figure 1d). Thus, the improvement in barotropic tides representation with a higher resolution model is not just due to the increase in horizontal resolution, but to the associated improvements in high-resolution bathymetry and coastline.

3. Surface signature of high-frequency motions

As mentioned in the introduction, one hypothesis for the steeper SSH wavenumber spectra slope in the equatorial region in the models than in observations is that the models underestimate high frequency motions. One measure of the surface manifestation of the high-frequency non-barotropic motions is the standard deviation of the steric SSH within a short period of time (order of days). Figures 2a-b display the monthly averaged standard deviation of the steric SSH calculated daily from hourly snapshots of NEATL and NEATL-HB. One can see that, for these two non-tidal experiments, the elevated high-frequency variability is concentrated along the western boundary current system, i.e., from the Florida Current to the Gulf Stream and further downstream to the North Atlantic Current in the subtropical North Atlantic, and the east/west Greenland current and Labrador current in the western subpolar North Atlantic. This high-frequency variability is induced by the small displacement of the boundary current/jet and by the generation and propagation of mesoscale to sub-mesoscale eddies/filaments. The variability is generally weak in the equatorial region, although still noticeably higher than that in the low-EKE region such as the eastern North Atlantic Ocean (Figures 2a-b).

For comparison with Figures 2a-b, Figures 2c-e displays the annual standard deviation for the three experiments with tides: NEATL-T, NEATL-T-HB, and NEATL-T-HB-HF. The inclusion of internal tides dramatically increases the high-frequency variability, particularly in the equatorial region. The increase is quite large off the Amazon shelf (near the equator), where internal tides are generated off the shelf break and propagate northeast and eastward into the open ocean (Jackson,

2004, 2007; Magalhaes et al., 2016), and around several bathymetry features/hot spots of the eastern North Atlantic basin, i.e., the Sierra Leone Rise (~5°N), the Cape Verde islands (~15°N, Ray and Zaron, 2016), and the Atlantis-Meteor Seamount Complex/Azores islands (30-36°N) (Löb et al., 2020; Zhao et al. 2016). The variability is also increased in the western boundary current around the New England seamounts chain (NESC). Internal tides there are generated on the northern edge of the Georges Bank in the outer Gulf of Maine and propagate southeastward (Brickman and Loder, 1993). The resolution of the bathymetry has a significant impact on the SSH variability near the internal tide generation hot spots (Figures 2c-d). Inclusion of high-frequency atmospheric forcing has little or no impact on the steric SSH variability (Figures 2d-e) indicating that high-frequency motions induced by wind variability of 1-6 hours (e.g., inertial motions) are ageostrophic and have a small or no SSH signature.

To quantitatively document the differences, Figure 3 displays the high-frequency steric SSH variability averaged in the equatorial region between 5°S and 5°N for the five experiments. The standard deviation value in this latitudinal band is ~0.5 cm in the two experiments without tides and three times as much in the three experiments with tides. While the standard deviation value is roughly the same in the open ocean interior for the three tidal experiments, it is nearly double near the western boundary off the Amazon shelf in the experiments with high-resolution bathymetry (NEATL-T-HB and NEATL-T-HB-HF).

To further illustrate the local impact of the high-resolution bathymetry, Figures 4a-b display modeled SSH snapshots from experiments NEATL-T-HB and NEATL-T, with the model bathymetry contours of 100, 1000, 2000, 3000, and 4000 m overlaid. Both experiments clearly show two rays of internal tides (solitary-like waves) with one propagating north-northeastward and the other east-northeastward into the open ocean. The wave crests of the internal tides are

however much more sharply defined in the simulation with high-resolution bathymetry (NEATL-T-HB). The north-to-northwestward propagating wave is illustrated in Figures 4c-d with a Hovmöller diagram of the SSH along the red dashed line in Figures 4a-b. The train of internal solitary-like waves starts right off the shelf near 100 m isobath and propagates north to northeastward, with a phase speed of about 2.8 m/s. Figures 4c-d also shows that the internal tides are much stronger in the experiment with high-resolution bathymetry (NEATL-T-HB).

The realism of the modeled internal tides can be assessed by comparing the model results to tidal signals (Figures 5a-b) captured off the Amazon shelf (red box in Figures 4a and b) by the Moderate Resolution Imaging Spectroradiometer (MODIS) sensors onboard the NASA's Earth observing system satellites (e.g., Jackson, 2004, 2007) and by the advanced synthetic aperture radars (ASAR) onboard the European Space Agency (ESA)'s Envisat (e.g., Magalhaes et al., 2016). The MODIS and ASAR images have a nominal resolution of 250 and 75 m respectively. The modeled wavelength of the internal tides (~120 km) is on the lower end of the observed wavelength (120-150 km) computed from the above images.

The question then arises as to what bathymetric features contribute to the differences between NEATL-T and NEATL-T-HB internal tides signatures. Internal tides are internal gravity waves generated in stratified waters by the interaction of barotropic tidal currents with variable bottom topography - key parameters are the horizontal scale, the slope, and the height of the topography (Garrett and Kunze, 2007). The modeled internal tides are generated at the shelf break close to the 100 m isobath (Figure 4), which is consistent with the observations of Jackson et al. (2004) and Magalhaes et al. (2016). Figure 6a displays the modeled vertical profile of the potential density in the deep ocean (at 45°W, 3°N) off the Amazon shelf. The model profile agrees well with the ocean climatology MIMOC (Schmidtko et al., 2013), with a strong pycnocline between 100 and 150 m

(maximum gradient of 0.045 kg/m^3 per meter in model versus 0.055 kg/m^3 per meter in MIMOC). Figure 6b shows the model bathymetry along the red line in Figures 4a-b. Even though the overall bathymetry is quite similar between NEATL-T and NEATL-T-HB, a closer look near the shelf break shows a significantly steeper slope in the experiment with high-resolution bathymetry included: from 1 to 1.2°N (the shaded area in the insert panel Figure 6c), the slope increases sharply from 0.001 (i.e., 1 m depth change over 1 km) to 0.065 in NEATL-T-HB, compared to a much smaller increase from 0.005 to 0.015 in NEATL-T. The slope of the bathymetry plays an important role in the generation of internal tides – intense beams of internal tidal energy are expected near "critical slopes" at which the bottom slopes equal to the ray slope (Garrett and Kunze, 2007). Using parameters that are characteristic of the Amazon Shelf region (i.e., an internal tide frequency $\omega \approx 1.4 \times 10^{-4}$ s^{-1}, a Coriolis parameter $f \approx 2.5 \times 10^{-6}$ s^{-1}, and a Väisälä frequency $N \approx 2.2 \times 10^{-2}$ s^{-1}), we can derive the resulting "critical slope" value to be ~0.063, which is on the same order of magnitude of the steeper slope found in NEATL-T-TB.

Overall, internal tides are stronger in the equatorial region than in the rest of the Atlantic basin because of the combination of stronger barotropic tides and stronger stratification. In the Atlantic Ocean, barotropic tides are strong in the equatorial region (from the Amazon shelf to west Africa) and along the eastern and northern rim of the North Atlantic basin, whereas they are rather weak in the western side of the North Atlantic, i.e., the Caribbean Sea, the Gulf of Mexico, and the majority of the US-Canada coastline. In the equatorial region, the stratification is driven by strong surface heating and strong Ekman upwelling which leads to a strong thermocline and pycnocline and a shallow, warm, and light mixed layer (Figure 6a). South of 15°S or north of 15°N, the thermocline or the pycnocline is significantly weaker and the mixed layer is denser and deeper than in the equatorial region.

4. Impact of tides, bathymetry, and high-frequency atmospheric forcing on SSH spectra

As shown in Figure 2, the inclusion of tides increases the high-frequency variability in steric SSH in the entire equatorial Atlantic region. Here we examine how this modifies the slope of the SSH wavenumber spectra in comparison to the observations. As in Zhou et al. (2015), we compute the slope of SSH spectra within the mesoscale range of 70-250 km in 10×10° boxes (with a 5° overlap) in the Atlantic Ocean from 20°S to 60°N. Figure 7 displays the slopes for the five experiments as well as the slopes computed from altimetry of Zhou et al. (2015). As already stated in the introduction, experiments without tidal forcing (such as NEATL and NEATL-HB) exhibit very little variability meridionally in the power spectra slope (Figures 7e and 7f) while the observed spectrum slopes are low/flat (in the order of 0.5-1) in the equatorial region, high/steep (in the order of ~5) in the western boundary current, and modestly high (3-4) in the eastern North Atlantic as well as toward the high latitudes (Figure 7a). The inclusion of tidal forcing in NEATL-T, NEATL-T-HB, and NEATL-T-HB-HF) leads to a dramatic reduction in the power spectra slopes in the equatorial region (from ~4 to ~1) as well as some flattening in the eastern North Atlantic (Figures 7b, c, and d, Figure 8d), a pattern that is consistent with the observations (Figures 7a). The latter is quantified by computing the difference in power spectra slopes between the observations and NEATL-T-HB-HF (Figure 8a). More than 50% of the boxes have a slope difference less than 0.5 and more than 90% of the boxes have a slope difference less than 1. Many of the large difference are in the coastal regions and/or marginal seas, where the number of usable altimetry tracks is significantly reduced; the uncertainty of the results for these coastal regions is therefore larger. The impact of high-frequency atmospheric forcing (Figure 8b) and high-resolution bathymetry (Figure 8c) on the SSH power spectra slopes is quantified by computing the slope differences between NEATL-T-HB-HF and NEATL-T-HB (Figure 8b) and between NEATL-T-HB and

NEATL-T (Figure 8c), respectively. The differences in power spectral slopes due to high-frequency atmospheric forcing (Figure 8b) and high-resolution bathymetry (Figure 8c) are relatively small when compared to the impact of internal tides (Figure 8d), which significantly flattens the slopes in the equatorial region; there is however some flattening of the spectral slope in the equatorial region off the Amazon Shelf due to the high-resolution bathymetry (Figure 8c). All five experiments, with or without tides, exhibit slightly lower slopes in the high latitudes than at mid-latitudes as in the observations (Figure 7). This flattened slope is not associated with internal tides but is a consequence of the reduction in the size of mesoscale eddies with latitude due to a decreasing baroclinic Rossby radius (e.g., Chelton et al. 2011). As a result, the spectra in the high latitudes start to level off near 250 km, and that leads to slightly flattened slopes for the fixed 70-250 km range.

It is important to note that the spectral slope is an overly simplified measure of the wavenumber spectra. To develop a more complete picture of the SSH variability across scales, one needs to look at the structure of the wavenumber spectra in the 70-250km range. In the remainder of this section, we examine how the modeled wavenumber spectra in the equatorial region compares with observations. One-dimensional SSH fields are computed from the modeled hourly snapshots along the Topex/Poseidon (T/P) tracks within 10×10° boxes, the latter to match the Zhou et al. (2015) computations from observations. Figure 9 displays four such boxes in the equatorial Atlantic (35-15°W, 10°S-10°N). The corresponding SSH spectra from the simulation NEATL-T-HB-HF are displayed in Figure 10. The colored curves are the SSH spectra calculated from individual tracks that are longer than 500 km in the 10×10° boxes. The black curve in each panel represents the average of all the spectra computed from the individual tracks over a 10×10° box. For comparison, the average observed spectra over the same 10×10° boxes are also shown in Figure 10 (circled

black curve) for filtered SSH data (Zhou et al., 2015). In all four boxes, the modeled SSH spectra exhibit two 'peaks' as in observations near 120 km (the characteristic internal tide wavelength shown in Figure 4) and 70 km (internal tide second mode) and a 'valley' in 150-500 km range. The modeled characteristic wavelength for first and second modes internal tides are consistent with that of the 1/25° global simulations as reported by Buijsman et al. (2020, their Figure 1). The 'valley' is not as distinct in the observations, especially in Figure 10b. One possibility for the model-data difference is that the model outputs are for one year only and do not have interannual variability. Toward small scales (less than 50 km in particular), the modeled spectra are noticeably lower than in observations. This could be dues to missing higher mode internal waves in the model or remaining noise in the observations.

The results are summarized in Figure 11 in which the SSH wavenumber spectra in the equatorial Atlantic (average of the four 10×10° boxes shown in Figure 9) of the five 1/50° HYCOM experiments are compared to the observations of Zhou et al. (2015) (filtered and unfiltered for noise) and Dufau et al. (2016). A couple of points can be made from this comparison. First, the inclusion of internal tides elevates the spectral energy level in the mesoscale and sub-mesoscale range to a level that is very similar to that based on the filtered SSH of Zhou et al. (2015), whereas the addition of high-resolution bathymetry and high-frequency atmospheric forcing does not change the SSH spectral levels significantly. Second, as pointed out by Zhou et al. (2015), in addition to instrumental errors, the SSH measured by satellite contains random and high-frequency noises that are spatially/temporally incoherent. Zhou et al. (2015) used a spatiotemporal filter based on empirical orthogonal functions (EOF) to remove these high-frequency noises while maintaining other high-frequency motions such as internal tides. The good agreement between the models and the Zhou et al (2015) filtered spectra appears to support the premise of Zhou at al.

(2015)'s noise removal. The SSH spectra in Dufau et al. (2016), which are based on more recent satellite observations (Jason-2, Cryosat-2, and SARAL/Altika), are essentially the same as the unfiltered results in Zhou et al. (2015), suggesting that their observations/results contain similar noises as in the TOPEX/Poseidon data used in Zhou et al. (2015).

5. One-dimensional versus two-dimensional SSH sampling

Satellite altimetry measures the SSH globally and repeatedly. This, however, comes with a caveat. The high-resolution observations are taken on 1-D tracks that are far apart (315 km at the equator for T/P), such that only a tiny fraction of the field is effectively sampled (Figure 9) with a multiple day repeat cycle (~10 days for T/P). In this section, we use the modeled SSH to investigate the sensitivity of the SSH power spectra to temporal/spatial sampling using the 25-15°W, 10°-0°S box (10×10°, see Figure 9) as an example.

To examine the impact of the temporal sampling, the modeled SSH spectra is computed for each of the 15 T/P 1-D tracks that go through the 10×10° box using SSH sampled every hour, as in our model, or every 238 hours, as in the T/P time sampling pattern. The latter essentially decreases the amount of SSH data by 2 orders of magnitude and leads to yearly SSH spectra that are noisier than the ones computed from the hourly snapshots (not shown). However, when the individual tracks of SSH spectra are averaged over the 10×10° box, the spectra are nearly identical (hourly and 10-day) (Figure 12a), suggesting that temporal sampling is not a determining factor in the computation of the average SSH power spectra.

To investigate the impact of spatial sampling, we now compare the SSH spectra computed hourly as above from the 15 T/P tracks (black curves, Figure 12b) and from ~500 zonal/meridional sections at full model resolution (~2 km at the equator) (red/blue curves for zonal/meridional, respectively, Figure 12b). We find that the SSH spectrum based on T/P tracks is closer to that of

the meridional than zonal sections, which is not surprising since the T/P tracks are oriented more meridionally than zonally in the equatorial region. Also, the energy level of the zonal SSH spectrum is lower than the meridional one. This can be attributed to the fact that that the equatorial circulation is primarily zonal and thus with less SSH variability in the zonal direction. If one considers the average of the zonal and meridional spectra as representative of the box, then sampling along the T/P tracks slightly overestimates the SSH spectrum, because of the orientation of the tracks.

The question then arises as to whether 1-D spectra are truly representative of the SSH variability, given that the wavenumber spectra based on zonal/meridional sections are different. When two-dimensional (2-D) fields are available, the conventional approach is to derive the 2-D spectrum with respect to both the zonal and meridional wavenumber components k and l as in Figure 13a and then to integrate the 2-D spectrum along a constant isotropic wavenumber k' that is defined as the square root of $k^2 + l^2$. The 2-D spectrum (Figure 13a), computed from the 10×10° box model outputs, is quite isotropic and hence supports the convention of generating 1-D spectra along the isotropic wavenumber k'. This 2-D derived spectra (pink line in Figure 13b) differ significantly from the 1-D spectra computed from SSH along T/P tracks (black line in Figure 13b) or along the zonal and meridional sections (blue line in Figure 13b). The energy level of the 2-D based spectra is generally higher, with a larger magnitude of the 'peaks' and 'valleys'. These differences are entirely due to different integration approaches. The integration along isotropic wavenumber preserves the highs and lows of the 2-D spectrum, whereas integration along constant k and l smooths out these 'peaks' and 'valleys' (equivalent to the 1-D spectra for the zonal and meridional sections of Figure 12b). Given the fact that the observational studies typically use the 1-D approach (e.g., Xu and Fu, 2011, 2012; Zhou et al., 2015; Dufau et al., 2016) whereas modeling studies

typically use the 2-D approach (e.g., Sasaki and Klein, 2012; Li et al., 2015; Chassignet and Xu; 2017), it is important to point out that they are not identical. For the equatorial box considered, the SSH spectrum slope is -1.0 calculated based on 2-D approach (along rotational wavenumber), compared to -1.1 and -1.2 based on 1-D approach using T/P tracks and zonal/meridional sections, respectively.

6. Summary and Discussion

Motivated by the discrepancy between a) the large spatial variability in the slopes of observed SSH power spectra (e.g., Xu and Fu, 2012; Zhou et al., 2015; Dufau et al. 2016) and b) the lack of comparable spatial variability in previously published high-resolution model results (e.g., Chassignet and Xu, 2017), this study systematically investigates the impacts of internal tides, high-resolution bathymetry, and high-frequency atmospheric forcing on the SSH wavenumber spectra in the Atlantic Ocean using a series of high-resolution (1/50°) Atlantic simulations validated against observations. We show that:

1) The inclusion of internal tides increases high frequency SSH variability (with peaks near 120 km and 70 km) and primarily flattens the spectral slope in the mesoscale range in the equatorial Atlantic, but also in the subtropical region in the eastern North Atlantic, all in good agreement with altimetric measurements. The internal tide is especially strong in the equatorial Atlantic when compared to higher latitudes because of both stronger barotropic tides and stronger stratifications in the upper water column.
2) High-resolution bathymetry plays an important role in internal tide generation on a local scale, although its impact on large-scale SSH variability and SSH wavenumber spectra is relatively small. High-frequency atmospheric forcing plays a minor role in high-frequency SSH variability. It should be noted that the high-frequency wind variability may have a

larger impact on the KE power spectra (than SSH), since some of these high-frequency motions (such as the near-inertial waves) are ageostrophic and do not have a corresponding SSH signature.

Since the SSH wavenumber spectral slope can be heavily impacted by high-frequency motions such as internal tides and gravity waves, the spatial variability of the observed spectrum slopes within the mesoscale range (e.g., Xu and Fu, 2012; Zhou et al., 2015; Dufau et al., 2016) may not be the most reliable measure as of which dynamical explanation, i.e., QG or SQG, is pertinent to describe the variability of SSH or KE/EKE of geostrophically balanced motions in the ocean, unless such internal gravity wave influences are properly removed. Throughout this paper, we have defined the mesoscale as the wavelength range between 70 and 250 km to be consistent with the previous observational and modeling studies. The spatial variability of the SSH spectral slope within this fixed mesoscale range (Figure 7) is in large part due to the fact that the transition scale varies throughout the basin between the geostrophically balanced flow and unbalanced motions. The transition scale is estimated to be less than 40 km in the western boundary current, on the order of 40-100 km in the interior of subtropical/subpolar regions, and greater than 200 km in the tropics (e.g., Qiu et al., 2017, 2018; Torres et al., 2018). One can therefore derive SSH spectra slope within a mesoscale range that varies geographically (e.g., Vergara et al., 2019).

One also needs to be aware that the SSH spectra computed from 1-D altimetry tracks can differ significantly from that based on the full 2-D field. We should point out that Ray and Zaron (2016) did calculate 2-D wavenumber spectra of the M_2 internal tides from observations, by including multiple satellite missions with different ground tracks to alleviate the under-sampling issue. The 2-D spectra were computed in three 20×20° regions of the Pacific Ocean and showed similar structures to those of our Figure 13a, except noisier with a less visible 2nd mode signature. They

did not compare the spectra computed from 2-D fields versus spectra computed from the 1-D tracks only. The Surface Water and Ocean Topography (SWOT) program soon will be able to measure the SSH in a 2-D swath of ~120 km wide, and that will significantly enhance our capability to quantify the SSH variability in 2-D and to understand the impacts of high-frequency motions on SSH variability.

Data Availability Statement

The full-resolution model outputs are stored in the U.S. Army Engineer Research and Development Center (ERDC) and U.S. Navy DoD Supercomputing Resource Center (DSRC) archive server. The model and altimetry-based spectra from Zhou et al (2015) (kindly provided by X. Zhou) are available in the data repository (http://doi.org/10.5281/zenodo.6462632).

Acknowledgement

XX, EPC, and AJW acknowledge support from Office Naval Research (ONR) grants 13034596 and N00014-19-1-2717 and from the National Aeronautics and Space Administration (NASA) grant 80NSSC20K1135. BKA acknowledges support from NASA grant 80NSSC20K1135 and ONR grant N00014-19-1-2712. MCB and MS acknowledges support from ONR grant N00014-19-1-2704 and NASA grant 80NSSC20K1135. The high-resolution HYCOM simulations were performed on supercomputers at the U.S. Army Engineer Research and Development Center (ERDC) in Vicksburg, Mississippi, and the U.S. Navy DoD Supercomputing Resource Center (DSRC) in Stennis Space Center, Mississippi, using computer time provided by the U.S. DoD High Performance Computing Modernization Program.

Reference:

Ansong J., Arbic B., Buijsman M., Richman J., Shriver J., & Wallcraft A. (2015). Indirect evidence for substantial damping of low-mode internal tides in the open ocean, *Journal of Geophysical Research: Oceans, 120*, 6057-6071, https://doi.org/10.1002/2015JC010998

Arbic, B. K., Wallcraft, A. J., & Metzger, E. J. (2010). Concurrent simulation of the eddying general circulation and tides in a global ocean model, *Ocean Modelling*, *32*, 175–187.

Arbic, B. K., Richman, J. G., Shriver, J. F., Timko, P. G., Metzger, E. J., & Wallcraft, A. J. (2012). Global modeling of internal tides within an eddying ocean general circulation model. *Oceanography*, 25(2):20–29, https://doi.org/10.5670/oceanog.2012.38.

Arbic, B. K., Alford, M. H., Ansong, J. K., Buijsman, M. C., Ciotti, R. B., Farrar, J., et al. (2018). A Primer on Global Internal Tide and Internal Gravity Wave Continuum Modeling in HYCOM and MITgcm. *New Frontiers In Operational Oceanography*, 307-391. available at: https://aquila.usm.edu/fac_pubs/15680.

Biri, S., Serra, N., Scharffenberg, M. G., & Stammer, D. (2016). Atlantic sea surface height and velocity spectra inferred from satellite altimetry and a hierarchy of numerical simulations. *Journal of Geophysical Research: Oceans, 121*, 4157–4177, https://doi.org/10.1002/2015JC011503.

Bleck, R. (2002). An oceanic general circulation model framed in hybrid isopycnic-Cartesian coordinates. *Ocean Modelling*, *4*, 55−88, https://doi.org/10.1016/S1463-5003(01)00012-9.

Blumen, W. (1978). Uniform potential vorticity flow. Part I: Theory of wave interactions and two-dimensional turbulence. *Journal of Atmospheric Science, 35,* 774–783.

Brickman, D., & Loder, J. W. (1993). Energetics of the Internal Tide on Northern Georges Bank, *Journal of Physical Oceanography, 23*, 409-424,

Buijsman, M. C., Arbic, B. K., Green, J. A. M., Helber, R. W., Richman, J. G., Shriver, J. F., et al. (2015). Optimizing internal wave drag in a forward barotropic model with semidiurnal tides. *Ocean Modelling, 85*, 42-55, https://doi.org/10.1016/j.ocemod.2014.11.003.

Buijsman M., Ansong J., Arbic B., Richman J., Shriver J., Timko P., et al. (2016). Impact of parameterized internal wave drag on the semidiurnal energy balance in a global ocean circulation model, *Journal of Physical Oceanography, 46,* 1399-1419, https://doi.org/10.1175/JPO-D-15-0074.1

Buijsman, M. C., Stephenson, G. R., Ansong, J. K., Arbic, B. K., Green, J. A. M., Richman, J. G., et ak, (2020). On the interplay between horizontal resolution and wave drag and their effect on tidal baroclinic mode waves in realistic global ocean simulations, *Ocean Modelling, 152*, https://doi.org/10.1016/j.ocemod.2020.101656.

Callies, J., & Ferrari, R. (2013). Interpreting energy and tracer spectra of upper-ocean turbulence in the submesoscale range (1–200 km). *Journal of Physical Oceanography*, *43*, 2456–2474, https://doi.org/10.1175/JPO-D-13-063.1.

Capet, X., Klein, P., Hua, B., Lapeyre, G., & McWilliams, J. (2008). Surface kinetic energy transfer in surface quasi-geostrophic flows. *Journal of Fluid Mechanics*, *604*, 165-174. https://doi.org/10.1017/S0022112008001110

Charney, J. G. (1971). Geostrophic Turbulence, *Journal of Atmospheric Science*, *28* (6), 1087-1095

Chassignet, E. P., Smith, L. T., Halliwell, G. R., & Bleck, R. (2003). North Atlantic simulations with the Hybrid Coordinate Ocean Model (HYCOM): Impact of the vertical coordinate choice, reference pressure, and thermobaricity. *Journal of Physical Oceanography, 33*, 2504–2526

Chassignet, E. P., & Xu, X. (2017). Impact of horizontal resolution (1/12° to 1/50°) on Gulf Stream separation, penetration, and variability. *Journal of Physical Oceanography, 47*, 1999−2021, https://doi.org/10.1175/JPO-D-17-0031.1.

Chassignet, E. P., & Xu, X. (2021). On the importance of high-resolution in large scale ocean models. *Advance in Atmospheric Science*, 38(10), 1621-1634, doi:10.1007/s00376-021-0385-7.

Chelton, D. B., Schlax, M. G., & Samelson, R. M. (2011). Global observations of nonlinear eddies. *Progress in Oceanography*, *91*, 166–216, https://doi.org/10.1016/j.pocean.2011.01.002.

Ducet, N., Le Traon, P. Y., & Reverdin, G. (2000). Global high resolution mapping of ocean circulation from the combination of TOPEX/POSEIDON and ERS-1/2. *Journal of Geophysical Research: Oceans*, *105*, 19,477–19,498.

Dufau, C., M. Orsztynowicz, G. Dibarboure, R. Morrow, & P.-Y. Le Traon, 2016: Mesoscale resolution capability of altimetry: Present and future. *Journal of Geophysical Research: Oceans*, *121*, 4910–4927, https://doi.org/10.1002/2015JC010904.

Egbert, G. D., & Erofeeva, S. Y. (2002). Efficient inverse modeling of barotropic ocean tides, *Journal of Atmospheric and Oceanic Technology* 19.2 183-204.

Ferrari, R., & Wunsch, C. (2009). Ocean circulation kinetic energy: Reservoirs, sources and sinks. *Annual Review of Fluid Mechanics*, *41*, 253–282, https://doi.org/10.1146/annurev.fluid.40.111406.102139

Ferrari, R., & Wunsch, C. (2010). The distribution of eddy kinetic and potential energies in the global ocean. *Tellus*, 62A, 92–108. 92-108, https://doi.org/10.1111/j.1600-0870.2009.00432.x

Fratantoni, D. M. (2001). North Atlantic surface circulation during the 1990's observed with saterllite-tracked drifters, *Journal of Geophysical Research: Oceans*, *106* (C10), 22,067-22,093, https://doi.org/10.1029/2000JC000730

Fu, L.-L. (1983): On the wave number spectrum of oceanic mesoscale variability observed by the SEASAT altimeter. *Journal of Geophysical Research: Oceans*, *88*, 4331–4341, https://doi.org/10.1029/JC088iC07p04331.

Garrett, C. & Kunze, E. (2007). Internal tide generation in the deep Ocean, *Annual Review of Fluid Mechanics, 39*, 57-87, https://doi.org/10.1146/annurev.fluid.39.050905.110227

Held, I. M., Pierrehumbert, R. T., Garner, S. T., & Swanson, K. L. (1995). Surface quasi-geostrophic dynamics. *Journal of Fluid Mechanics*, 282, 1–20.

Hua, B. L., & Haidvogel, D. B. (1986). Numerical simulations of the vertical structure of quasi-geostrophic turbulence. *Journal of Atmospheric Science*, 43, 2923–2936.

Isern-Fontanet, J., Chapron, B., Lapeyre, G., & Klein, P. (2008). Potential use of microwave sea surface temperatures for the estimation of ocean currents. *Geophysical Research Letters, 33*, L24608, https://doi.org/10.1029/2006GL027801.

Jackson, C. R. (2004). An Atlas of Internal Solitary-like Waves and their Properties. 2nd ed. Global Ocean Associates, 560 pp. [Available online at http://www.internalwaveatlas.com/Atlas2_index.html]

Jackson, C. R. (2007). Internal wave detection using the Moderate Resolution Imaging Spectroradiometer (MODIS), *Journal of Geophysical Research: Oceans*, *112*, C11012, https://doi.org/10.1029/2007JC004220

Jayne, S. R., & St. Laurent, L. C. (2001), Parameterizing tidal dissipation over rough topography. *Geophysical Research Letters* 28, 811-814. https://doi.org/10.1029/2000GL012044

Lapeyre, G., & Klein, P. (2006). Dynamics of the upper oceanics layers in terms of surface quasigeostrophy theory. *Journal of Physical Oceanography*, 36, 165–176. https://doi.org/10.1175/JPO2840.1

LaCasce, J., & Mahadevan, A. (2006). Estimating subsurface horizontal and vertical velocities from sea surface temperature. *Journal of Marine Research*, *64*, 695–721. https://doi.org/10.1357/002224006779367267

Le Traon, P. Y., Rouquet, M., & Boissier, C. (1990). Spatial scales of mesoscale variability in the North Atlantic as deduced from Geosat data. *Journal of Geophysical Research: Oceans*, *95*, 20 267–20 285, https://doi.org/10.1029/JC095iC11p20267.

Le Traon, P. Y., Klein, P., Hua, B. L., & Dibarboure, G. (2008). Do altimeter wavenumber spectra agree with the interior or surface quasigeostrophic theory? *Journal of Physical Oceanography*, *38*, 1137–1142, https://doi.org/10.1175/2007JPO3806.1.

Li, Z., von Storch, J.-S., & Müller, M. (2015). The M 2 internal tide simulated by a 1/10° OGCM. *Journal of Physical Oceanography, 45*, 3119–3135, https://doi.org/10.1175/JPO-D-14-0228.1

Löb, J., Köhler, J., Mertens, C., Walter, M., Li, Z., von Storch, J.-S., et al. (2020). Observations of the low-mode internal tide and its interaction with mesoscale flow south of the Azores. *Journal*

of Geophysical Research: Oceans, 125(11), e2019JC015879. https://doi.org/10.1029/2019JC01

Magalhaes, J. M., da Silva, J. C. B., Buijsman, M. C., & Garcia, C. A. E. (2016). Effect of the North Equatorial Counter Current on the generation and propagation of internal solitary waves off the Amazon shelf (SAR observations), *Ocean Science, 12*, 243–255, https://doi.org/10.5194/os-12-243-2016.

McWilliams, J. C. (1989). Statistical properties of decaying geostrophic turbulence. *Journal of Fluid Mechanics, 198* (1). 199-230. https://doi.org/10.1017/s0022112089000108

Ngodock, H. E., Souopgui, I., Wallcraft, A. J., Richman, J. G., Shriver, J. F., & Arbic, B. K. (2016). On improving the accuracy of the M2 barotropic tides embedded in a high-resolution global ocean circulation model. *Ocean Modelling 97*, 16-26, https://doi.org/10.1016/j.ocemod.2015.10.0

Paiva, A. M., Hargrove, J. T., Chassignet, E.P., & Bleck, R. (1999). Turbulent behavior of a fine mesh (1/12°) numerical simulation of the North Atlantic. *Journal Marine System*, *21*, 307–320.

Qiu, B., Chen, S., Klein, P., Wang, J., Torres, H., Fu, L.-L., & Menemenlis, D. (2018). Seasonality in transition scale from balanced to unbalanced motions in the world ocean. *Journal of Physical Oceanography, 48*(3), 591–605. https://doi.org/10.1175/JPO-D-17-0169.1

Qiu, B., Nakano, T., Chen, S., & Klein, P. (2017). Submesoscale transition from geostrophic flows to internal waves in the northwestern Pacific upper ocean. *Nature Communications*, *8*, 14055. https://doi.org/10.1038/ncomms14055

Ray, R. D. (1998). Ocean self-attraction and loading in numerical tidal models. *Marine Geodesy 21*, 181–192.

Ray, R. D., & Zaron, E. (2016). M2 internal tides and their observed wavenumber spectra from satellite altimetry. *Journal of Physical Oceanography*, *46*, 3–22, https://doi.org/10.1175/JPO-D-15-0065.1.

Richardson, P. L. (1983). Eddy kinetic energy in the North Atlantic from surface drifters. *Journal of Geophysical Research: Oceans*, *88*, 4355–4367.

Richman, J. G., Arbic, B. K., Shriver, J. F., Metzger, E. J., & Wallcraft, A. J. (2012). Inferring dynamics from the wavenumber spectra of an eddying global ocean model with embedded tides, *Journal of Geophysical Research: Oceans*, *117*, C12012, https://doi.org/10.1029/2012JC008364.

Rocha, C. B., Chereskin, T. K., Gille, S. T., & Menemenlis, D. (2016). Mesoscale to Submesoscale Wavenumber Spectra in Drake Passage, *Journal of Physical Oceanography*, *46*(2), 601-620. https://doi.org/10.1175/JPO-D-15-0087.1

Sasaki, H., & Klein, P. (2012). SSH wavenumber spectra in the North Pacific from a high-resolution realistic simulation. *Journal of Physical Oceanography*, 42, 1233–1241, https://doi.org/10.1175/JPO-D-11-0180.1.

Savage, A. C., Arbic, B. K., Alford, M. H., Ansong, J. K., Farrar, J. T., Menemenlis, D., et al. (2017). Spectral decomposition of internal gravity wave sea surface height in global models, *Journal of Geophysical Research: Oceans, 122,* 7803–7821, https://doi.org/10.1002/2017JC013009.

Schmidtko, S., Johnson, G. C., & Lyman, J. M. (2013). MIMOC: A global monthly isopycnal upper-ocean climatology with mixed layers, *Journal of Geophysical Research: Oceans*, *118*, 1658–1672, https://doi.org/10.1002/jgrc.20122.

Shriver, J. F., Arbic, B. K., Richman, J. G., Ray, R. D., Metzger, E. J., Wallcraft, A. J., & Timko, P. G. (2012). An evaluation of the barotropic andinternal tides in a high-resolution global ocean circulation model, *Journal of Geophysical Research: Oceans*, *117*, C10024, https://doi.org/10.1029/2012JC008170.

Smith, K. S., & Vallis, G. K. (2001). The scales and equilibration of midocean eddies: Freely evolving flow. *Journal of Physical Oceanography*, 31, 554–571.

Stammer, D. (1997). Global characteristics of ocean variability estimated from regional TOPEX/POSEIDON altimeter measurements. *Journal of Physical Oceanography*, 27, 1743–1769.

Tchilibou, M., Gourdeau, L., Morrow, R., Serazin, G., Djath, B., & Lyard, F. (2018). Spectral signatures of the tropical Pacific dynamics from model and altimetry: a focus on the meso-/submesoscale range, *Ocean Science, 14*, 1283–1301, https://doi.org/10.5194/os-14-1283-2018,

Torres, H. S., Klein, P., Menemenlis, D., Qiu, B., Su, Z., Wang, J., et al. (2018). Partitioning ocean motions intobalanced motions and internal gravitywaves: A modeling study in anticipationof future space missions. *Journal of Geophysical Research: Oceans, 123*, 8084–8105. https://doi.org/10.1029/2018JC014438

Vergara, O., Morrow, R., Pujol, I., Dibarboure, G., & Ubelmann, C. (2019). Revised global wave number spectra from recent altimeter observations. *Journal of Geophysical Research: Oceans*, 124, 3523–3537. https://doi. org/10.1029/2018JC014844

Wang, D.-P., Flagg, C. N., Donohue, K., & Rossby, H. T. (2010). Wavenumber spectrum in the Gulf Stream from shipboard ADCP observations and comparison with altimetry measurements. *Journal of Physical Oceanography, 40*, 840–844, https://doi.org/10.1175/2009JPO4330.1.

Wunsch, C., & Stammer, D. (1995). The global frequency-wavenumber spectrum of oceanic variability estimated from TOPEX/POSEIDON altimetric measurements. *Journal of Geophysical Research: Oceans, 100*, 24 895–24 910.

Wyrtki, K., Magaard, L., & Hager, J. (1976). Eddy energy in the oceans, *Journal of Geophysical Research: Oceans*, *81*, 2641-2646

Xu, Y., & Fu, L.-L. (2011). Global variability of the wavenumber spectrum of oceanic mesoscale turbulence. *Journal of Physical Oceanography*, *41*, 802–809, https://doi.org/10.1175/2010JPO4558.1.

Xu, Y., & Fu, L.-L. (2012). The effects of altimeter instrument noise on the estimation of the wavenumber spectrum of sea surface height. *Journal of Physical Oceanography*, 42, 2229–2233, https://doi.org/10.1175/JPO-D-12-0106.1.

Zhao, Z., Alford, M. H., Girton, J. B., Rainville, L., & Simmons, H. L. (2016). Global Observations of Open-Ocean Mode-1 M2 internal tides, *Journal of Physical Oceanography, 46*, 1657-1684, https://doi.org/ 10.1175/JPO-D-15-0105.1

Zhou, X.-H., Wang, D.-P., & Chen, D. (2015). Global wavenumber spectrum with corrections for altimeter high frequency noise, *Journal of Physical Oceanography*, *45*(2), 495-503, https://doi.org/10.1175/JPO-D-14-0144.1.

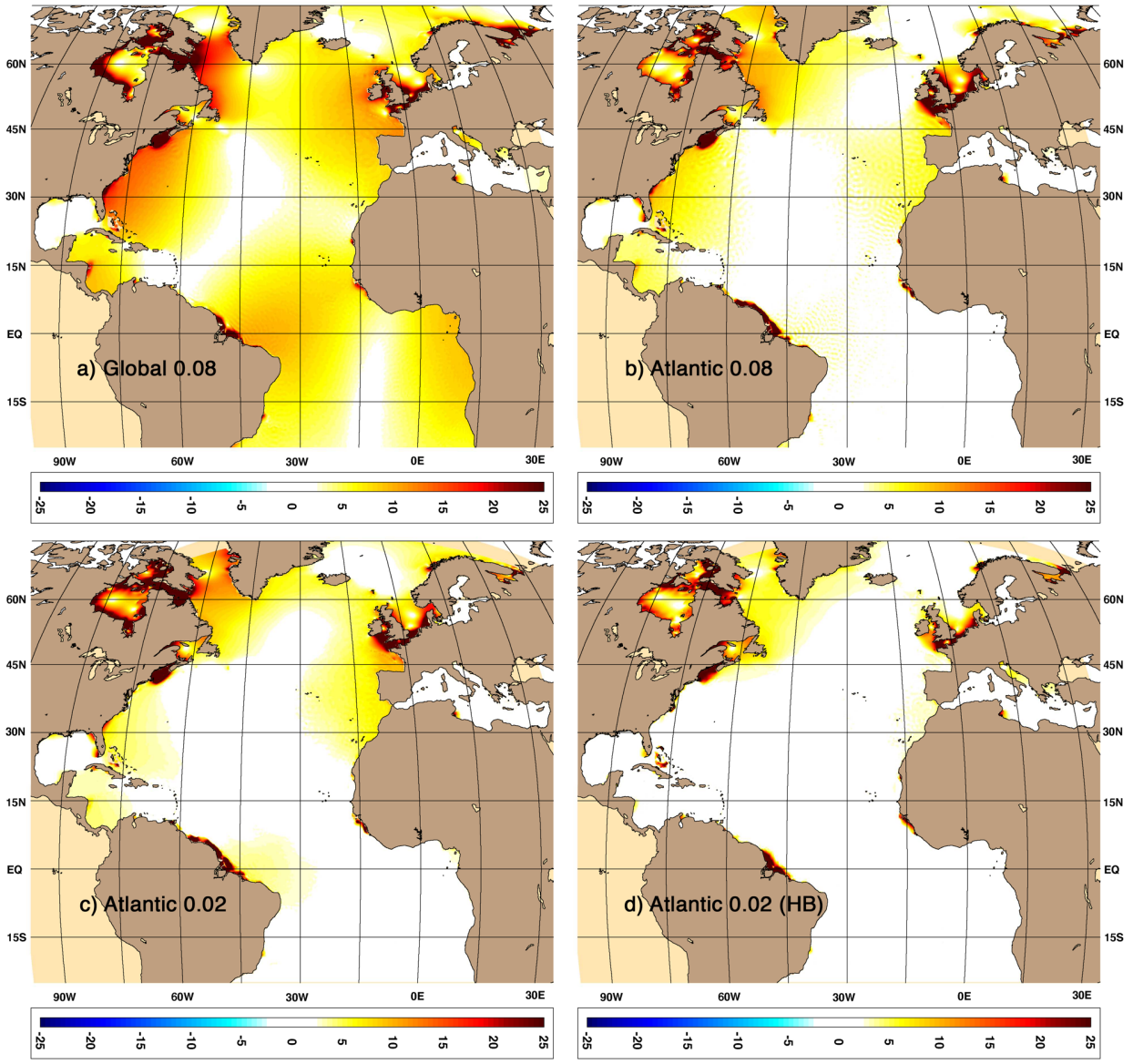

Figure 1. Root-square-mean (RMS) error in cm of the modeled barotropic M_2 tide in four HYCOM simulations compared to TPXO8: a) 1/12° Global simulation; b) 1/12° Atlantic simulation; c) 1/50° Atlantic simulation NEATL-T (with bathymetry interpolated from 1/12° simulation); and d) 1/50° Atlantic NEATL-T-HB (with bathymetry calculated from 30 arc-sec GEBCO_2019).

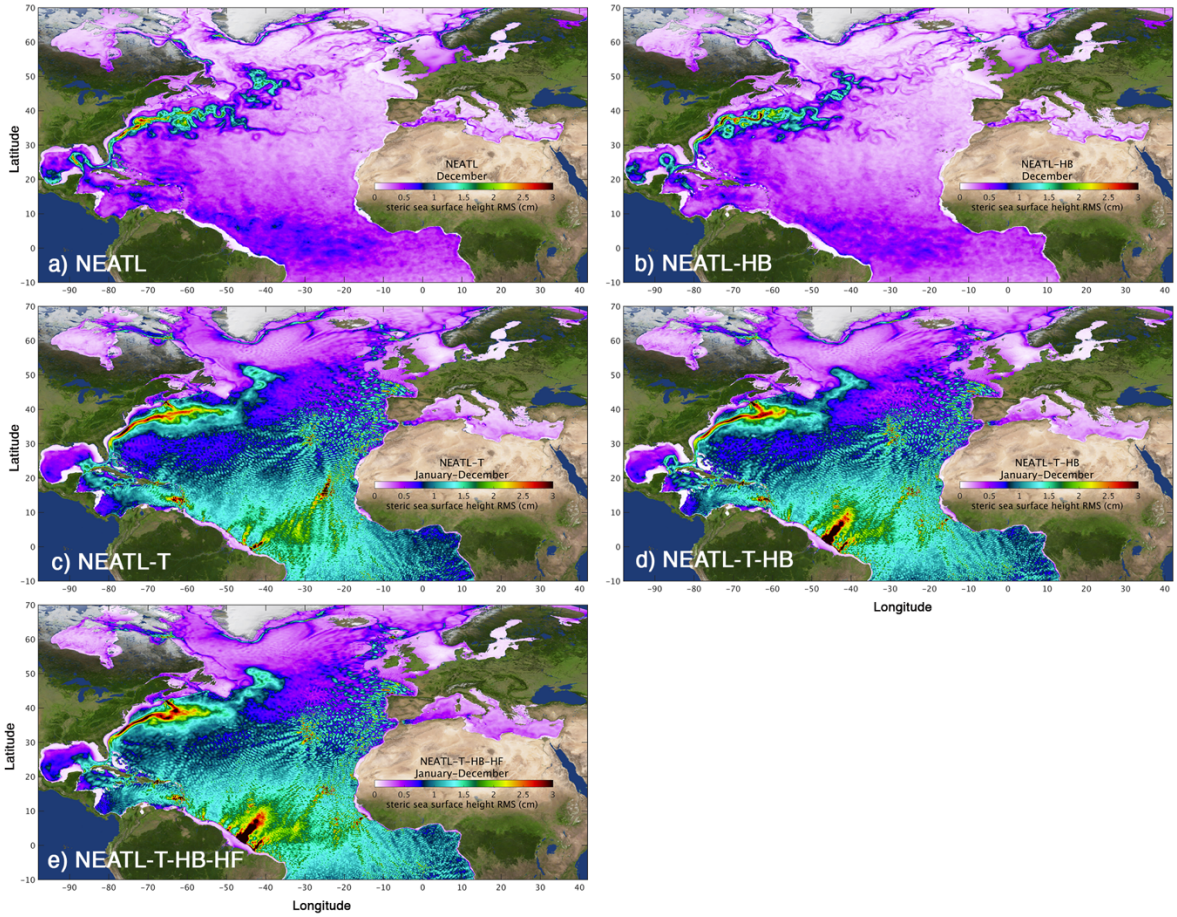

Figure 2. Standard deviation value of the modeled high-frequency steric sea surface height (SSH, in cm) variability in five 1/50° Atlantic simulations that are summarized in Table 1: a) NEATL, b) NEATL-HB, c) NEATL-T, d) NEATL-T-HB, and e) NEATL-T-HB-HF. The standard deviation is calculated from the hourly snapshots of the SSH within a day and averaged over one month for experiments a-b and over one year for experiments c-e (to reduce spatial noise).

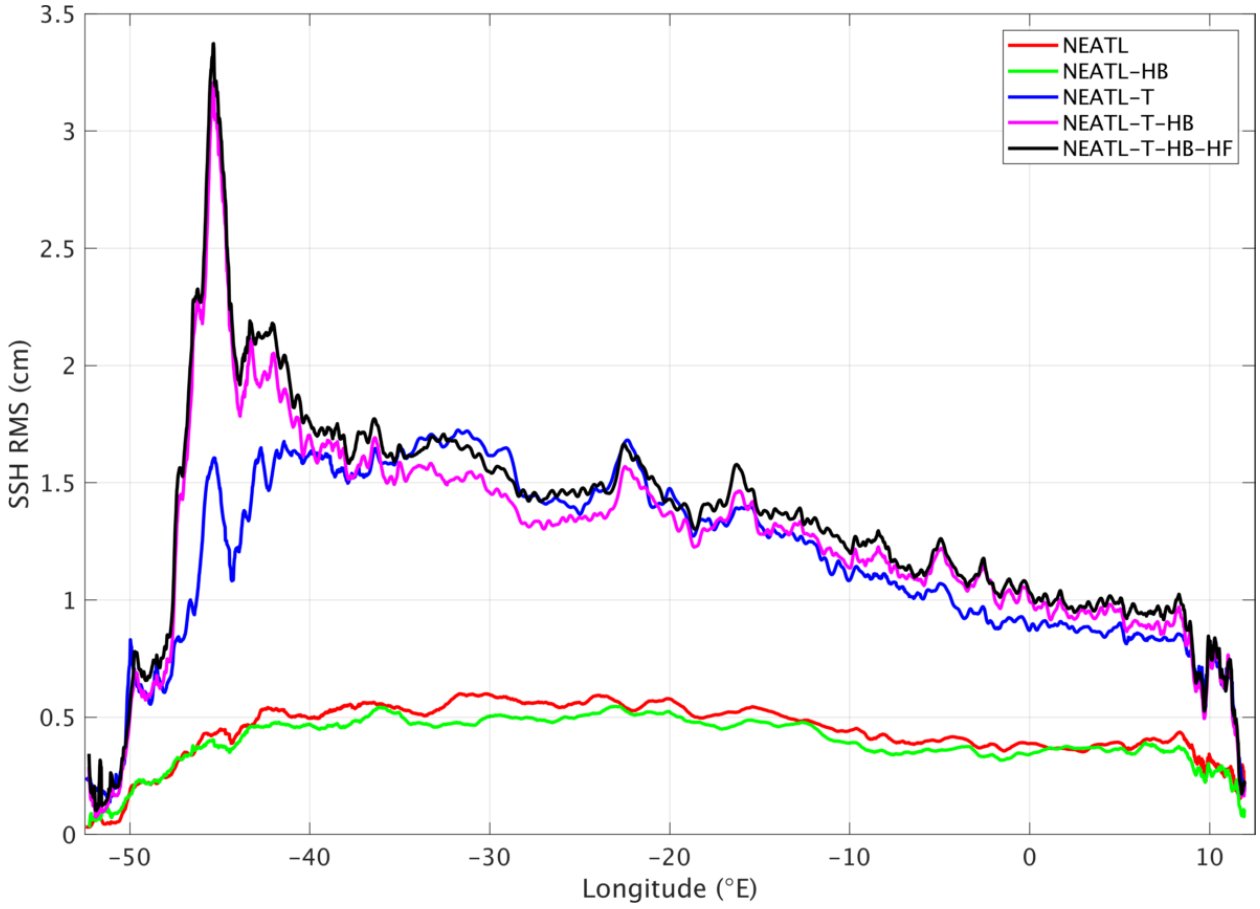

Figure 3. Standard deviation of the high-frequency steric sea surface height (SSH, in cm) variability in the equatorial Atlantic (averaged between 5°S and 5°N) in five 1/50° Atlantic simulations that are shown in Figure 2: a) NEATL, b) NEATL-HB, c) NEATL-T, d) NEATL-T-HB, and e) NEATL-T-HB-HF.

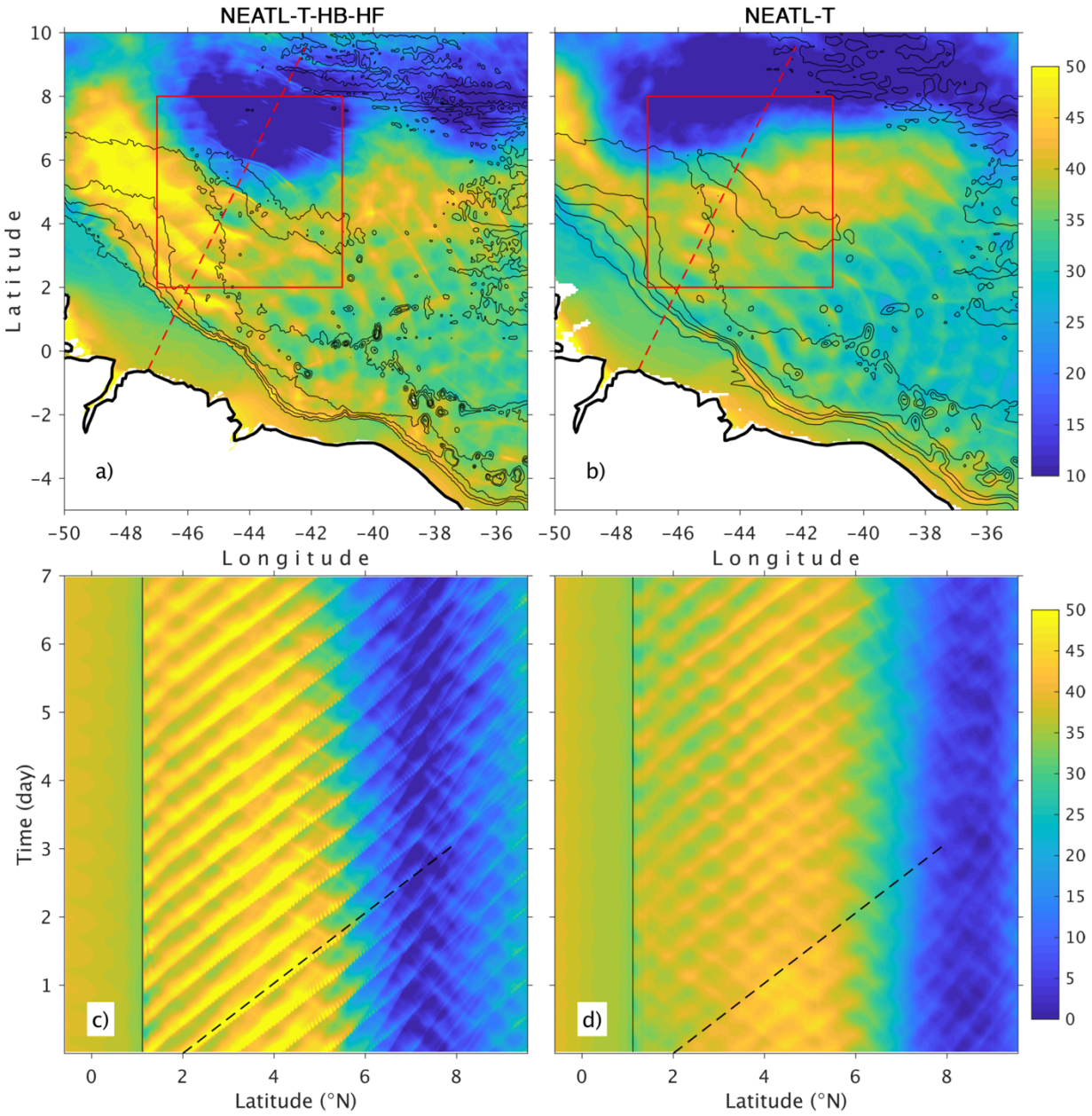

Figure 4. Internal tide generation off the Amazon shelf in two simulations with and without high-resolution bathymetry: NEATL-T-HB-HF (a & c), NEATL-T (b & d). Panels a-b show a snapshot of the steric SSH (in cm); panels c-d show a Hovmöller diagram of the steric SSH (in cm) along the dashed red line in panels a-b. Black solid line indicates the location of shelf break at 100-m isobath (see also the insert panel in Figure 6b) and black dashed line indicates a northward phase speed of 2.5 m/s.

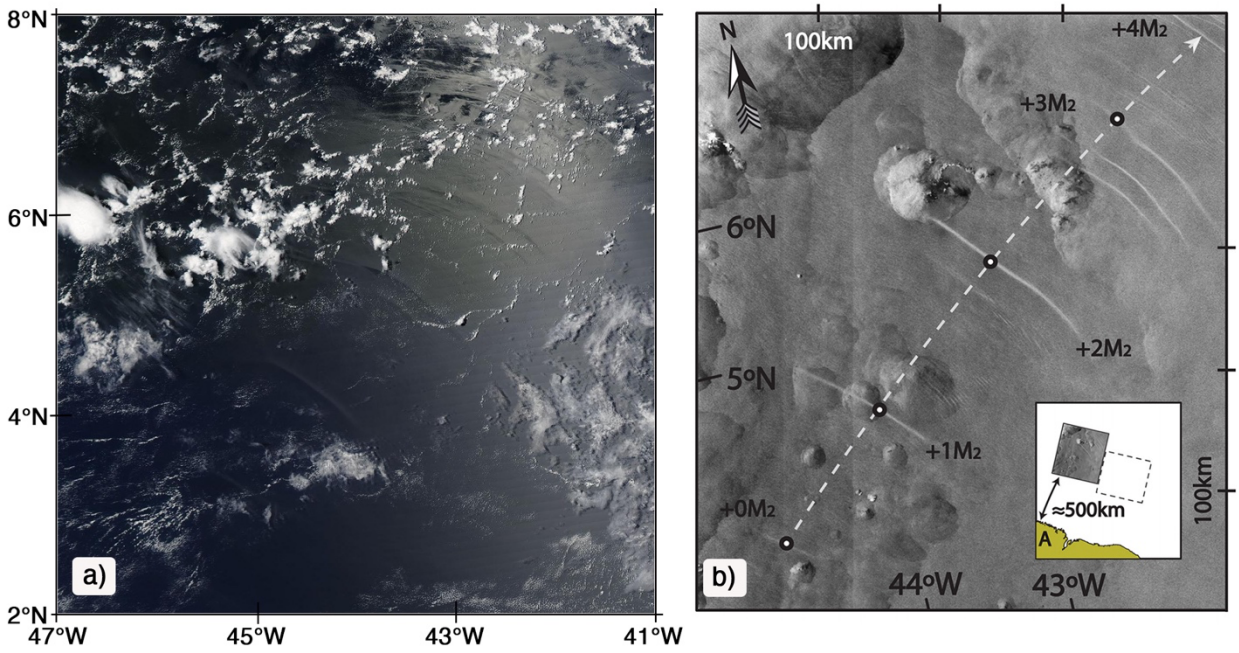

Figure 5. Surface signature of the internal tides in the western equatorial Atlantic: a) Subset of a moderate resolution imaging spectroradiometer (MODIS) image taken from *Aqua* on August 3rd, 2003 (Jackson 2004; available from NASA at https://worldview.earthdata.nasa.gov). The area of the image (6×6°) is indicated by a red rectangle in Figure 4a. b) Subset of an advanced synthetic aperture radar (ASAR) image taken from *Envisat* on February 2nd, 2011 (Magalhaes et al., 2016).

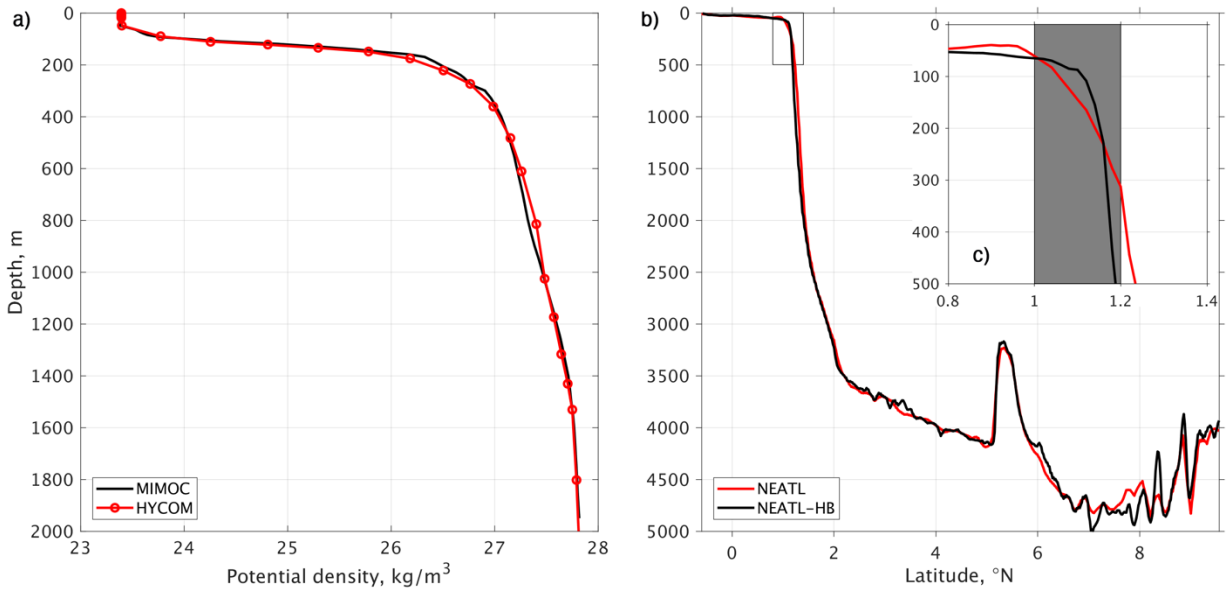

Figure 6. a) density profile off the Amazon shelf in 1/50° HYCOM simulation NEATL-T-HB-HF and in ocean climatology MIMOC (Schmidtko et al., 2013); b) The model bathymetry along a north-northeastward section from the Amazon shelf to the open ocean (dashed line in Figures 4a-b) in two 1/50° simulations with and without high-resolution bathymetry variability; the insert panel c) shows the bathymetry zoomed near the shelf break, as denoted by the small rectangle in panel b).

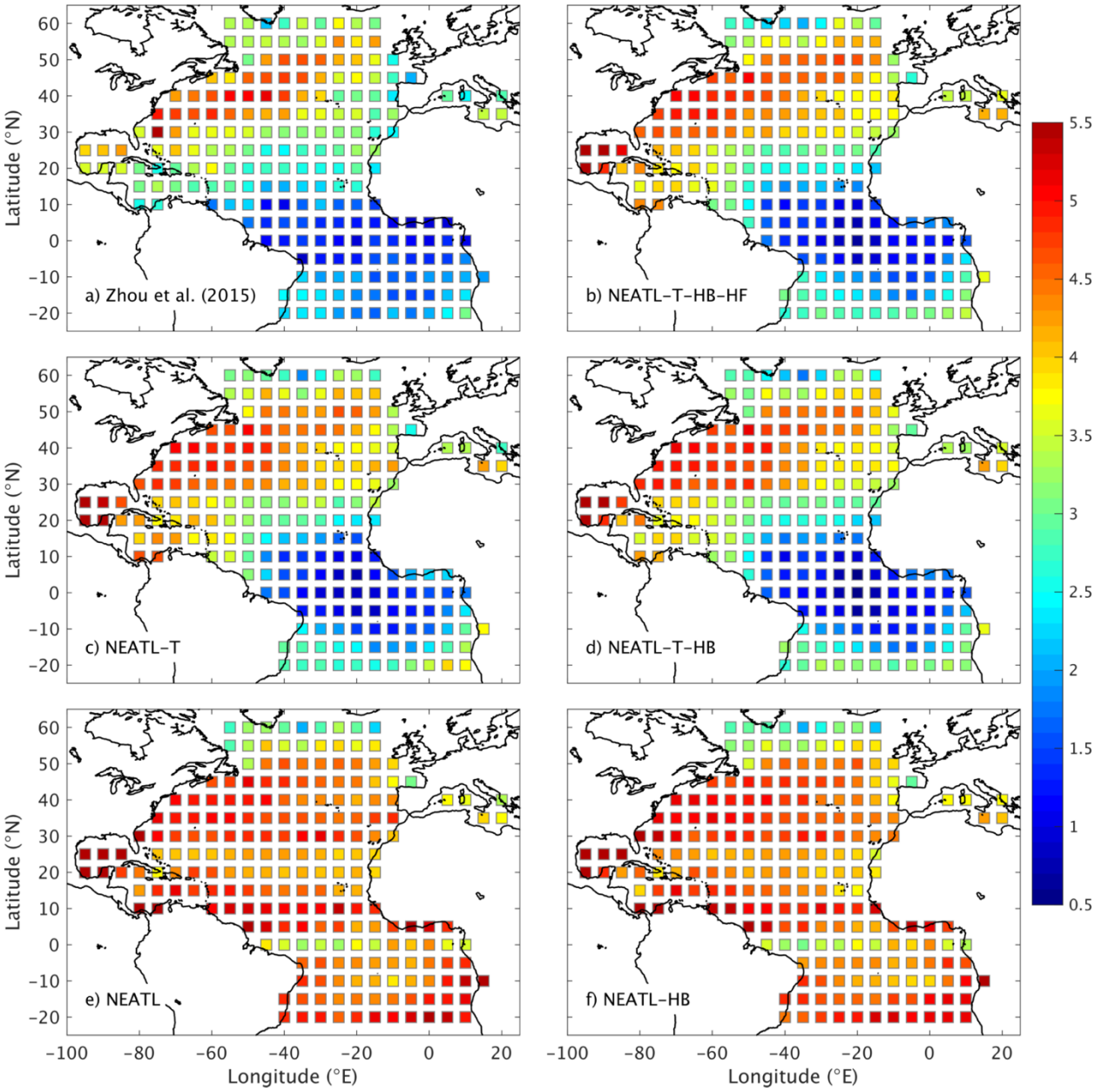

Figure 7. Slope of SSH wavenumber spectra in the Atlantic Ocean from observations (Zhou et al. 2015) and five Atlantic simulations. The slope is for mesoscale range (70-250 km) and the value is inversed (multiplied by -1).

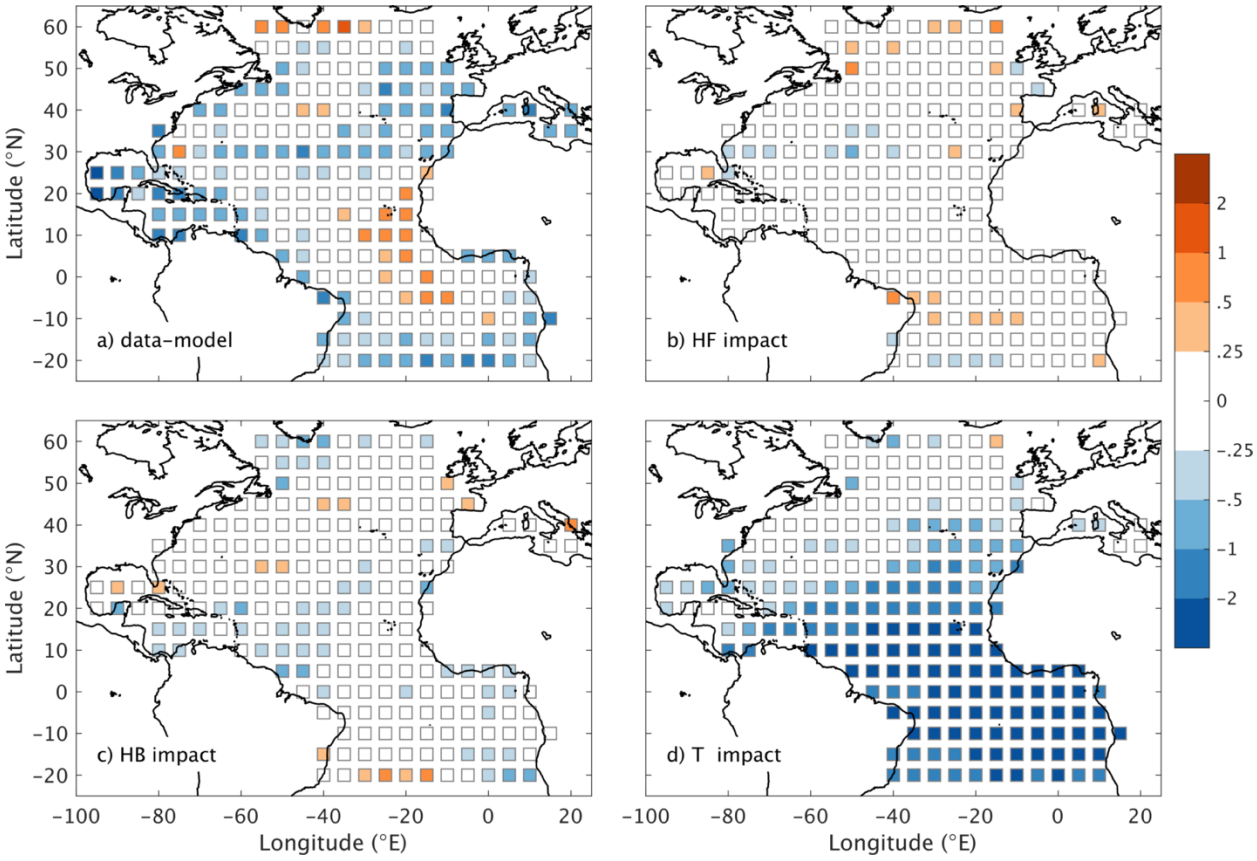

Figure 8. Difference of the spectra slope presented in Figure 7 to highlight a) the data-model difference (observations minus NEATL-T-HB-HF); b) the impact of high-frequency atmospheric forcing (NEATL-T-HB-HF minus NEATL-T-HB); c) the impact of high-resolution bathymetry (NEATL-T-HB minus NEATL-T); and d) the impact of tides (NEATL-T-HB minus NEATL-HB).

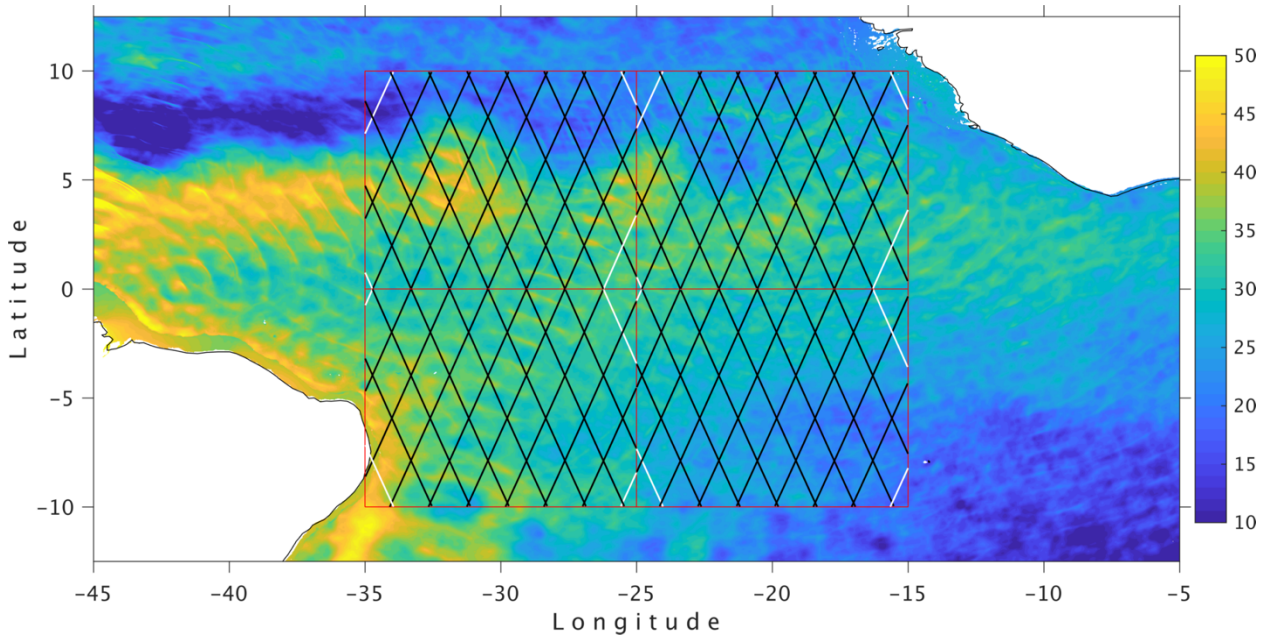

765

Figure 9. Topex/Poseidon (T/P) tracks in four 10×10° boxes in the equatorial Atlantic. The color shading displays a snapshot of the modeled steric SSH from NEATL-T-HB-HF. The black lines denote the nominal and interlaced T/P tracks in each box that are longer than 500 km and used for wavenumber spectra calculation; the white lines are the track segments that are shorter than 500 km and not used.

770

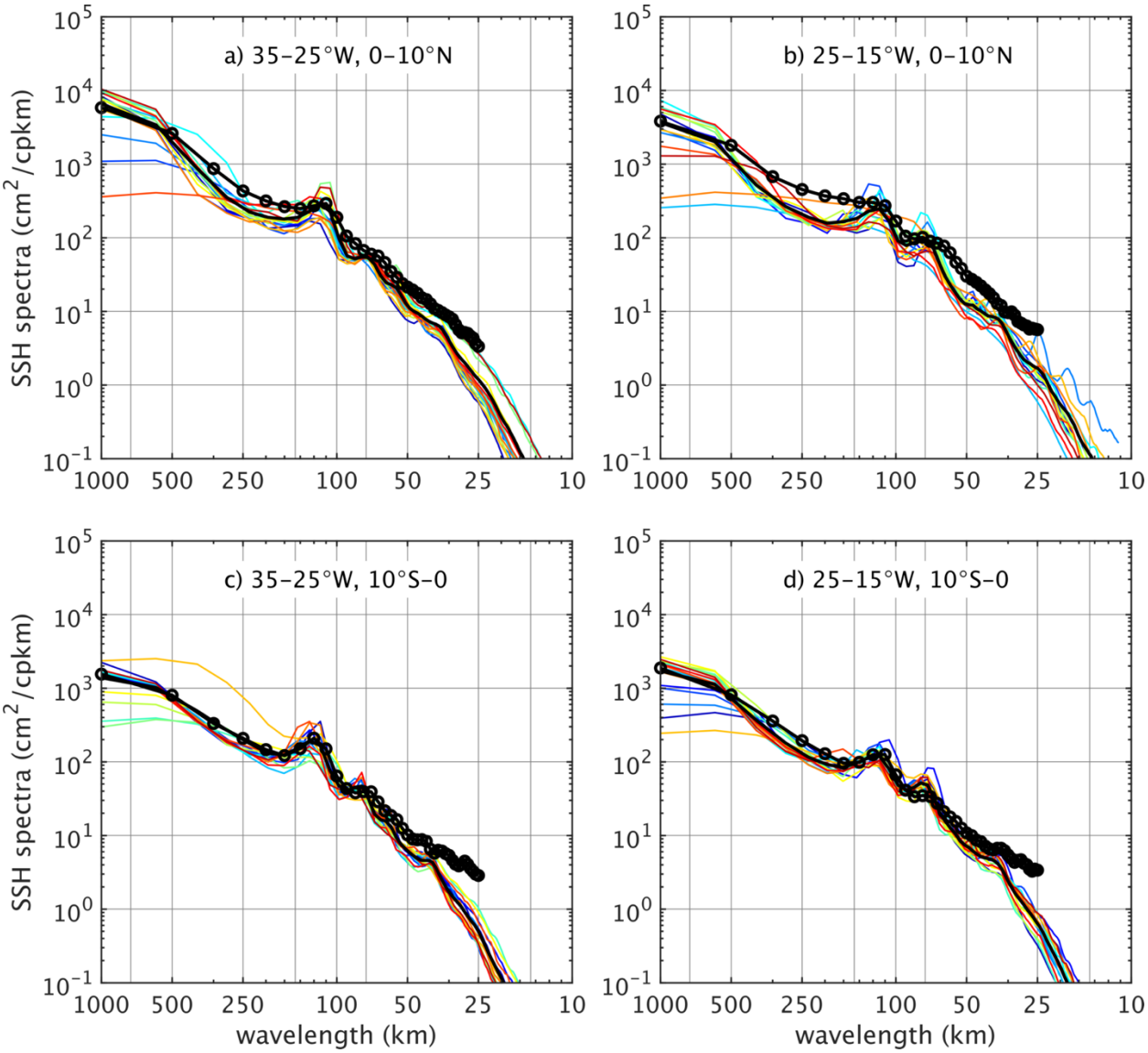

Figure 10. SSH wavenumber spectra calculated from T/P tracks in four 10×10° boxes in the equatorial Atlantic. The colored curves are modeled (NEATL-T-HB-HF) wavenumber spectra based on individual tracks and the black curves are their average, representing the modeled wavenumber spectra of the box. The circled black curves are the observation results from Zhou et al. (2015).

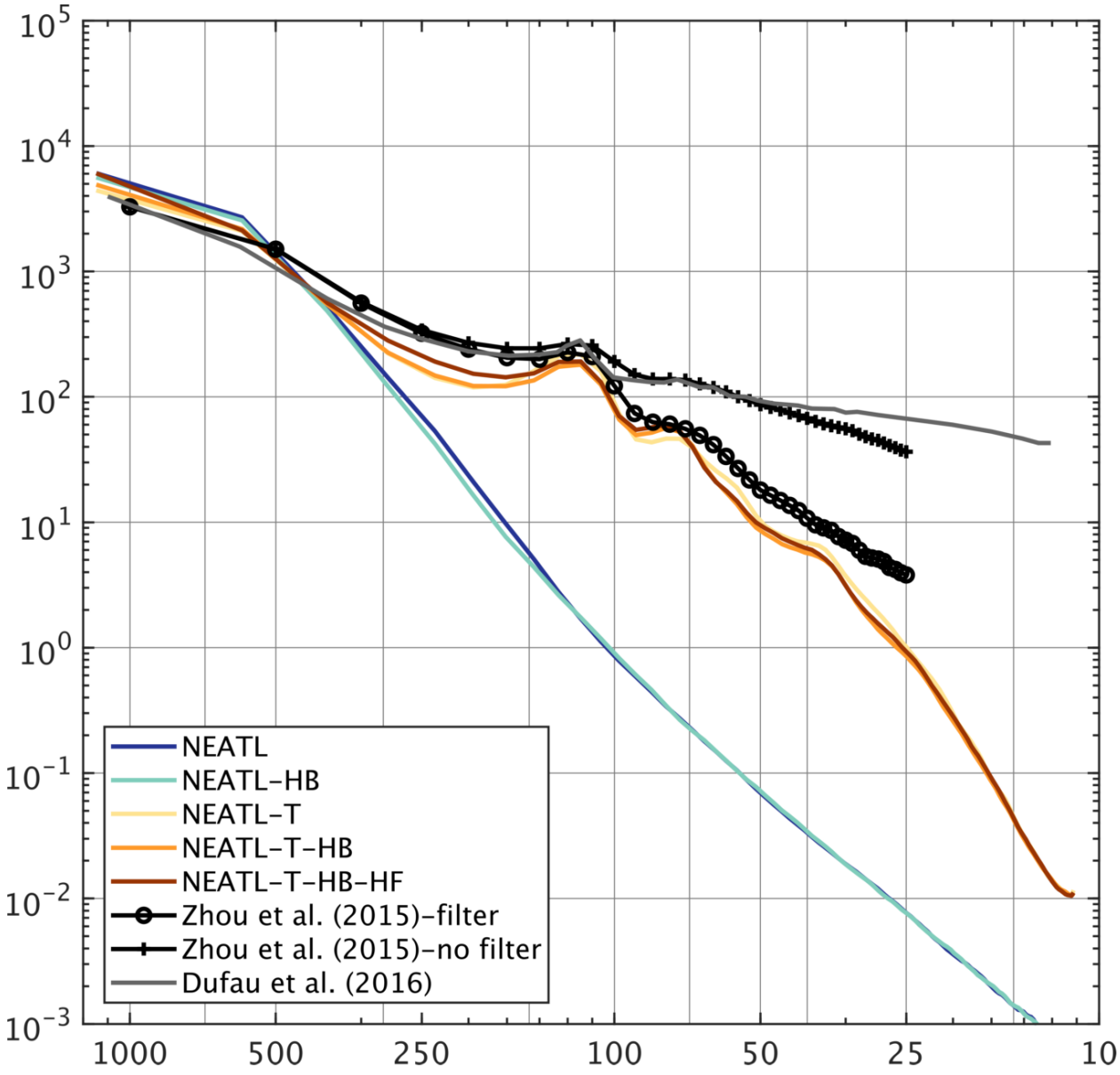

785 Figure 11. A comparison of the modeled and observed SSH wavenumber spectra in the equatorial Atlantic, averaged from four 10×10° boxes as shown in Figure 9. The results highlight the impact of internal tides in elevating SSH variability from mesoscale to sub-mesoscale to a level that is comparable to observations. The results also show that the more recent SSH measurements in Dufau et al. (2016) contain similar noise as the unfiltered data in Zhou et al. (2015).

790

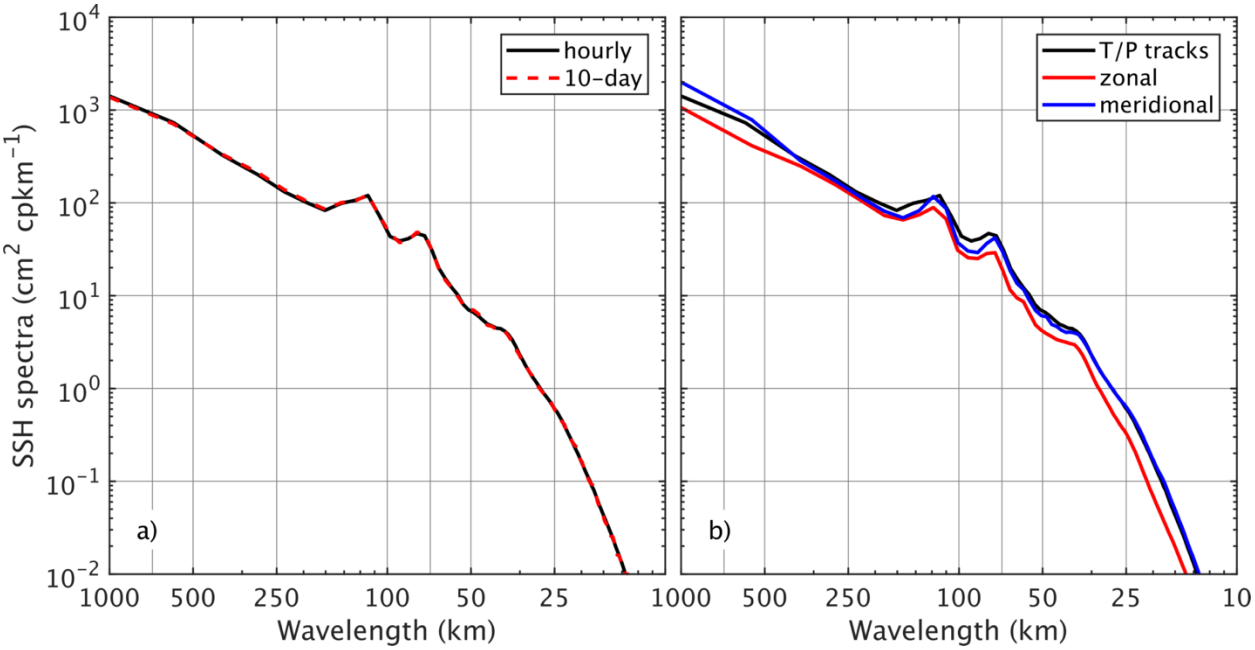

Figure 12. Impact of temporal/spatial sampling on SSH wavenumber calculation: panel a) shows the spectra calculated from tracks that are sampled every hour versus every 10 days; panel b) shows the spectra calculated from T/P tracks versus from zonal and meridional tracks with full model resolution.

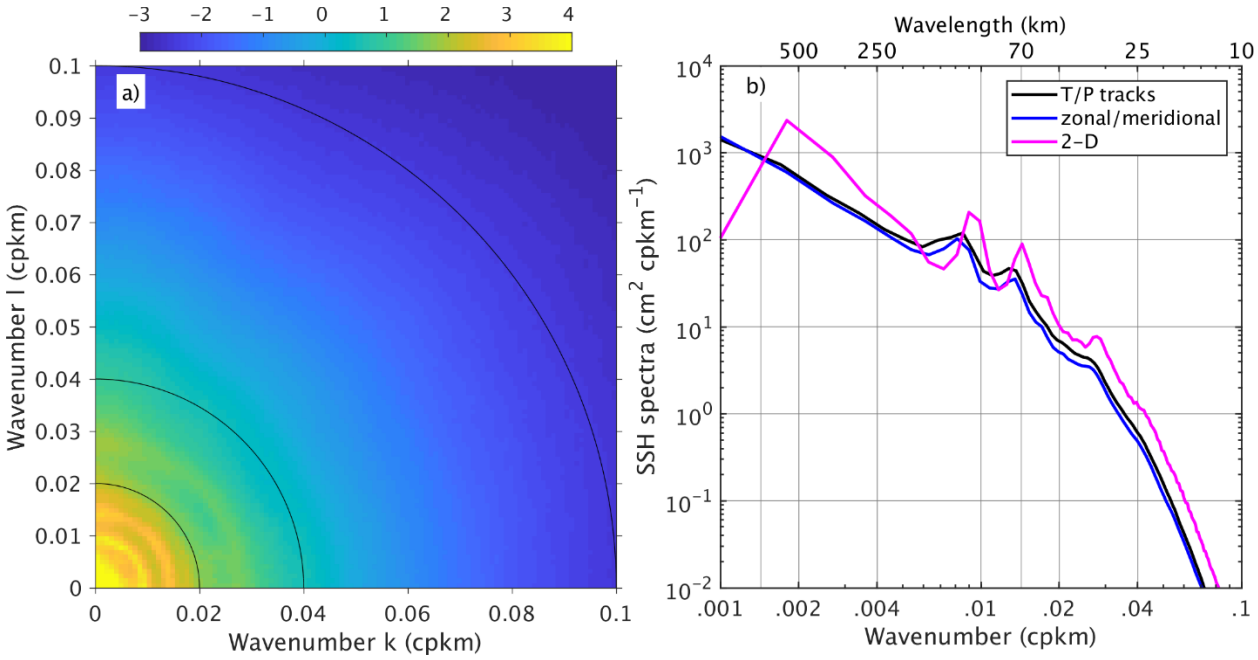

Figure 13. Impact of 1-D versus 2-D measurements on SSH wavenumber spectra calculation. Panel a) shows the 2-D wavenumber spectra calculated from the (2-D) SSH fields. Panel b) compares the wavenumber spectra computed from 1-D SSH field sampled along the T/P tracks (black) and along zonal/meridional sections (blue) and computed from the 2-D spectra in panel a) that is then projected onto the isotropic wavenumber $k' = \sqrt{k^2 + l^2}$.